ORIGINAL ARTICLE

Critical thermal shock temperature prediction of alumina using improved hybrid models based on artificial neural networks and Shannon entropy

B. Fissah[1,*], H. Belghalem[1], M. Djeddou[2] and B. Mamen[3]

[1] Department of Mechanical Engineering, Laboratoire des Mines, Larbi Tébessi University, 12000, Tébessa, Algeria.
[2] Department of Hydraulics, Larbi Ben M'hidi University, 04000, Oum El Bouaghi, Algeria.
[3] Department of Civil Engineering, Abbès Laghrour University, 40000, Khenchela, Algeria.

ABSTRACT – This study investigates the potential of a simple and Hybrid artificial neural network (ANN) to predict dense alumina's critical thermal shock temperature (ΔT_c). The predictive models have been constructed using two ANNS models (M1, M2). In the first model (M1), elaboration, physical and mechanical parameters have been exploited to build three ANNs, namely generalized linear regression (M1-GLRNN), extreme learning machine (M1-ELM), and radial basis function (M1-RBFNN). The second model (M2) has been built by the three models mentioned above incorporated by the Shannon Entropy (SE) method. To compare the performance of all the developed models, coefficient of correlation (R), root mean square error (RMSE), mean absolute percentage error (MAPE), and Nash-Sutcliffe efficiency coefficient (NSE) have been considered. It is found that M2-RBFNN model with (RMSE = 4.3526, MAPE= 0.3406, NSE = 0.9921, and R= 0.9960) had superiority to the M1-RBFNN model (RMSE = 4.7030, MAPE= 0.3003, NSE = 0.9908, and R = 0.9954). More importantly, the contribution of the present work is that prediction of ΔT_c has been performed through the developed hybrid model (M2-RBFNN), which reduces the number of inputs from six to only four inputs and offers high accuracy for all the studied variables.

INTRODUCTION

Thermal shock occurs when there is an abrupt change in the temperature of a material. The resulting temperature gradient develops gradient stresses that can locally reach the yield strength of the material and cause damage [1]. The thermal shock and thermal cycling effects are known to limit ceramics performance in many applications. Thermal shock resistance is often evaluated by measuring the resistance to fracture after the thermal shock (residual stress), making it possible to define a critical temperature range at which the material degrades.

Since the 1950s, many scientists have carried out various experimental and fundamental studies on the thermal shock resistance of ceramic materials [2-9]. Nevertheless, the crack propagation resulting from thermal shock is a speedy and complex procedure for these materials. The most commonly employed theories are the critical stress fracture theory [2] and the thermal shock damage theory [3]. It is essential to note that the thermal resistance properties of brittle materials such as alumina [4-6] and glass [7-9] have been extensively studied based on these two theories.

On the one hand, the first theory is derived from thermoelasticity and focuses on controlling the conditions of fracture nucleation. On the other hand, the second theory allows characterizing the critical temperature difference and the damage state of the material. The second theory considers the instability of pre-existing cracks according to the temperature difference.

Using the thermoelastic dynamics method, Hasselman inserted the thermal shock resistance parameter (R) to estimate the performance of a brittle ceramic material exposed to thermal shock loading. He concluded that R is correlated to the critical temperature through Eq. (1).

$$\Delta T_c = \psi^{-1}(\beta) \frac{(1-v)K_{1c}}{E\alpha Y\sqrt{\pi a_c}} \tag{1}$$

With α is the coefficient of expansion, E is Young's modulus, K_{1c} is the toughness, ΔT_c is the applied critical temperature difference, ψ is the stress reduction coefficient, β is the Biot number defining the severity of the thermal shock, v is Poisson's ratio, ac is the crack length and Y is a geometric constant. The first parameter (R) for a hard thermal shock (β very high and $\psi \cong 1$), is expressed through Eq. (2):

$$R = \Delta T_c = \frac{\sigma_R(1-v)}{E\alpha} \tag{2}$$

where σ_R is the fracture strength.

However, this model often used complex analyses for simple geometry. Consequently, several parameters characterizing thermal shock have been introduced. More recently, the principles of fracture mechanics are taken into account. The intensity coefficient for a geometrical case is estimated and then compared to the fracture properties [10].

There is an increasing need to establish reliable mathematical models to predict the impact of mechanical properties such as modulus of elasticity, tensile strength, toughness, imposed temperature difference, and material microstructure on thermal shock resistance.

It is essential to know the relationship between these parameters and their influence on thermal shock resistance. It is not easy to build an accurate model using conventional methods. Artificial neural networks (ANNs) have become a very efficient modeling technique, suitable for building complex and nonlinear models with high accuracy. Many parameters such as processing parameters and physical parameters can distress the thermal shock temperature of alumina.

Studying the thermal shock temperature of brittle materials, mainly ceramic materials, and testing different parameters is costly and time-consuming. Several studies in the literature use regression or artificial intelligence methods to predict the mechanical and thermal behavior of materials similar to ceramic materials. In the study carried out by Koker et al. [11], the effect of different training algorithms on the learning performance of neural networks on predicting the bending stiffness behaviour of reinforced particles (Al-Si-Mg)-MCs has been investigated. In contrast, the primary objective of this study is to predict the outcome of bending and hardness experiments for reinforced Al_2O_3/SiC. Their results show a good agreement between the neural network and the experimental results for each training method.

An artificial neural network model has been designed by Sheikh et al. to predict the properties (porosity, density, shrinkage, and surface area) of porous alumina prepared by the gel casting method [12]. The model input parameters are sintering temperature, yeast cell concentration, and soaking time, while the outputs are porosity, density, shrinkage, and surface area. They show that the results of the artificial neural network convincingly agree with the experimental data, and the artificial neural network provides valuable data.

In the study carried out by Shokuhfar et al., the mechanical properties of Al_2TiO_5 based ceramics using ANN have been predicted. They find that the Levenberg–Marquardt algorithm (LM) is much better than the others [13]. According to the results of ANN, one can predict the effect of talc addition on the bulk density of tialite and easily understand its composition.

Tool Huang et al [14] developed a three-layer neural network model to predict composite ceramic's bending strength and fracture toughness. It has been shown that the expected results are in good agreement with the measured value.

Elmabrouk and Kalkanlia have developed two models to predict the rate of acid erosion [15]. Multiple regression models and artificial neural networks (ANN) have been used to predict the amount of acid erosion rate. They compared the predictive ability of the two approaches. They conclude that the artificial neural networks are more accurate in predicting acid corrosion rate than the multiple regression model.

N. Altinkok [16] has applied the BP-ANN model to predict mechanical parameters such as density, tensile strength, and hardness of various metal matrix reinforced composites (MMC).

Adesina et al [17] have investigated the potential of (ANN) to forecast the mechanical properties (density and hardness) of graphene nanoplatelets (GNPs) developed under different processing conditions using the Spark Plasma Sintering technique (SPS). Similarly, Çöl et al [18] have applied an ANN to predict fracture toughness in micro-alloyed steel under industrial production conditions by measuring the impact energy of process properties. In addition, Zhang et al [19] have used (ANNs) and a genetic algorithm (GA) to calculate critical mechanical characteristics of ceramic matrix materials, such as hardness, bending strength, and fracture toughness. The content of the compositions determines the inputs, and the outputs are the mechanical properties.

The problem studied is the thermal shock temperature of alpha-alumina (α-Al2O3) using simple and hybrid artificial neural networks. The methods used in the present study are simple and hybrid artificial neural networks. Simple networks are radial based neural networks (RBFNN), generalized regression neural networks (GRNN), and extreme learning machines (ELM). However, hybrid networks are developed by combining the previous simple networks with the Shannon entropy (SE) method to reduce the input parameters.

Therefor, this work aims to find a model to predict the thermal shock temperature of alumina and then model the relationship between the first thermal shock parameter (R) and other properties (density, grain size, and Young's modulus), and processing parameters (holding time, sintering temperature and sintering pressure). By considering the properties of ANNs in the prediction procedure, models are proposed to predict the thermal shock temperature of micro-structured alumina. Then, the outcomes of the suggested ANN models (GRNN, ELM, RBFNN, and hybrid Shannon entropy method) are compared with experimental data.

According to the exiting literature and the authors' best knowledge, there is no research investigating the critical thermal shock temperature using a numerical approach. However, the experimental approach is financially costly and time-consuming. These limitations led us to develop artificial neural networks to predict the thermal shock temperature of ceramic materials.

Finally, the success of the developed models is analyzed and shows the potential of (RBFNN) for predicting the critical thermal shock temperature. The best accuracy of RBFNN predictions is obtained when reducing the input from six to four input parameters of the artificial neural network using Shannon's entropy method. In contrast, low accuracy is observed for GRNN and ELM predictions using six input parameters. Most importantly, the M2-RBFNN model provides high accuracy for all the studied parameters.

DATABASE AND METHODOLOGY

In this study, the data has been established from reference [20] and used to build the different models of ANNs. The samples are prepared using commercial alpha-alumina nanopowder with an average particle size of 150 nm. The sample's dimensions are consistent with the standard ones used in laboratory experiments. According to the flow chart shown in Figure 1, SPS sintering has been performed using an FCT sintering device (FCT HPD 25 System, Germany). The powders are loaded into a cylindrical graphite mould with an inner diameter of 50 mm. The samples are then heated under pressure. The sintering temperature varies between 1150 and 1350 °C. A pressure of 25-50 MPa is applied until the end of the waiting period. The obtained samples have a diameter of 50 mm and a thickness of 7 mm. Then, parallelepiped samples are cut from these disks. The final dimensions are (40×4×3) mm3. Tests have been performed on these samples to obtain the mechanical properties and the critical temperature of thermal shock. The experimental conditions such as sintering temperature, sintering pressure, and holding time, in addition to the obtained test results, are then used as inputs to build the predictive models for the critical temperature parameter of thermal shock (output).
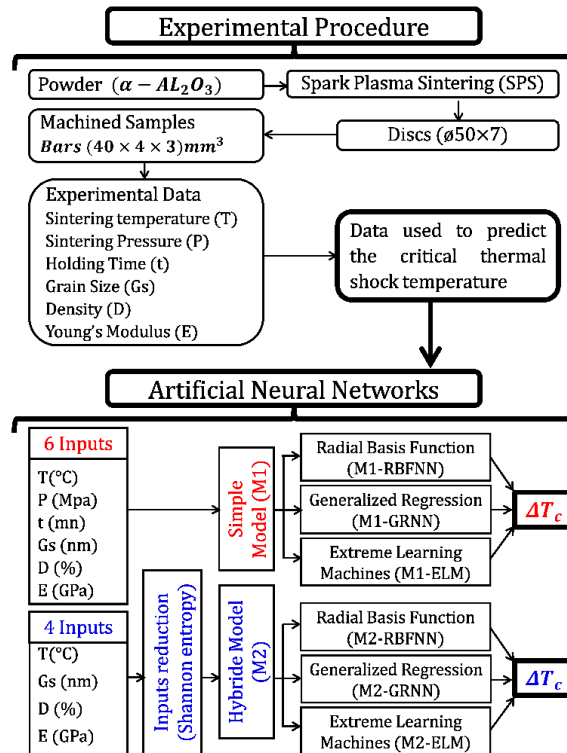
Figure 1. Procedural flow chart for numerical analyses used in the prediction of the critical thermal shock temperature of alumina

Samples Preparation

Scanning electron microscopy (SEM) has been used to examine the samples, where the impact of sintering pressure, temperature, and holding time on grain size has been investigated. The influence of these factors has been detailed in a previous study [21].

The apparent density of the samples is calculated by immersing them in distilled water according to Archimedes' principle. Also, Young's modulus of the samples is measured by a dynamic, non-destructive method from the transverse vibration frequency. Additionally, the fracture strength is measured before the thermal shock test using a four-point bending test. The samples are characterized according to the schematic illustration presented in Figure 2. The indented samples are held in an oven at a selected temperature for 10 minutes (hold time for homogenization). Then, its large faces are exposed to a jet of air at a temperature of $T_f = 20$ °C. The samples are characterized by a heat transfer coefficient of 600 $Wm^{-2}K^{-1}$. Several thermal cycles are performed by increasing the temperature of the oven [22].

Finally, the critical temperature is assessed through the Acoustic Emission (AE) spectrum. As shown in Figure 3, the single peak corresponds to the initiation of unstable propagation of the longitudinal crack. For the experimental conditions shown in Figure 3, the critical temperature is evaluated at T=715 °C.
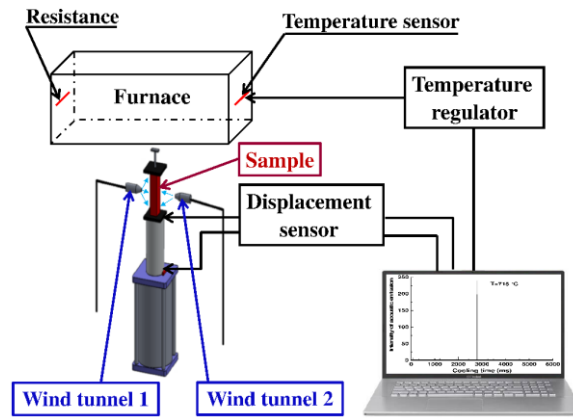
Figure 2. Thermal shock device
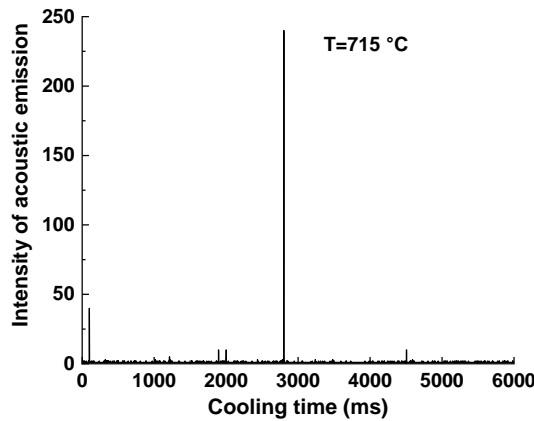
Figure 3. Acoustic emission spectra obtained during thermal shock for T=1150 °C, t=10 mn and P=50 MPa

Inputs used for the Construction of ANNs Models

The input parameters for determining the thermal shock temperature parameter (ΔTc) of the tested Alumina bars are the sintering temperature (T), holding time (t), pressure (P), relative density (D), grain size (G_s), and Young's modulus (E).

ARTIFICIAL NEURAL NETWORKS METHODS

Shannon's Theory of Entropy

Shannon [23] demonstrated that events with a high probability of occurrence provide reduced information. Conversely, if the probability of an occurrence is low, the obtained information is more significant. In this way, both uncertainty and the information of the parameters are connected. Entropy theory is used as an essential indicator to quantify the relevant elements. Figure 4 presents the crucial steps recommended in Shannon entropy theory.
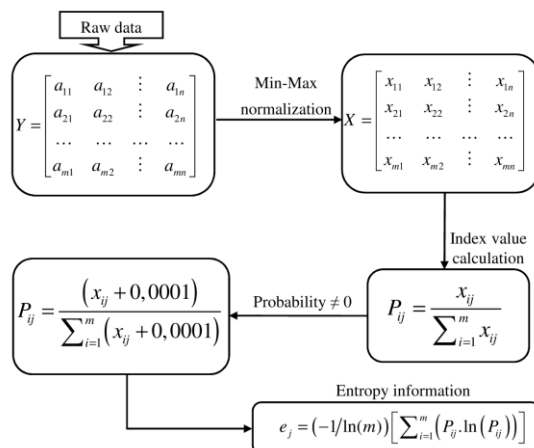
Figure 4. Flow chart of Shannon's entropy theory

Radial Basis Function Neural Network (RBFNN)

RBFNN is widely used for predictive modeling in various engineering domains [24-27]. RBFNN, as shown in Figure 5, is represented as a three-layer architecture. The first layer receives inputs. The second is the intermediate layer which contains a nonlinear RBF activation function. The third layer makes the prediction.
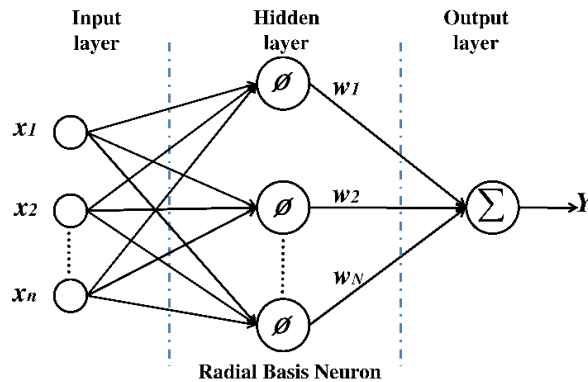
Figure 5. Model of RBFNN structure

The governing equation of the RBFNN output is expressed as follows:

$$y_i(x) = \sum_{j=1}^{k} w_{ij}\, \emptyset \lVert x - c_j \rVert \tag{3}$$

where x, y_i, k, c_j, w_{ij}, $\lVert\,.\,\rVert$ are the input vector, the output of the ith network, the number of neurons in the hidden layer, the center of the jth hidden neuron, the link weight from the jth neuron in the hidden layer to the ith neuron in the output layer, and the Euclidean norm, respectively. ϕ is the radial basis function used in the hidden layer neurons. The Gaussian function is the most commonly used RBF, defined as follows:

$$\emptyset(\lVert x - c_j \rVert) = exp\left(\left|-\frac{\lVert x - c_j \rVert^2}{2\sigma_j^2}\right|\right) \tag{4}$$

where σ_j is the width of the hidden neuron j^{th}.

To construct and train the RBFNN, the weights that connect the hidden neurons to the outputs, centers, and width are considered as essential keys. The dimension and distribution of input patterns influence the number of hidden neurons. As the dimension decreases, the number of hidden neurons decreases [28]. More information on RBFNN is presented in [29].

Generalized Regression Neural Network (GRNN)

Specht [30] suggested generalized regression neural networks (GRNN). It is a variety of RBNNs based on kernel regression [31,32]. One of the advantages of this network is its consistency. It is a high coherence network and can obtain near-zero estimation error for an extensive training set with simple limitations on the function. The GRNN architecture is shown in Figure 6. It does not need an iterative learning process like back-propagation networks. Therefore, the estimation of the function can be derived from the training data and easily approximates any arbitrary function between the input and output data.
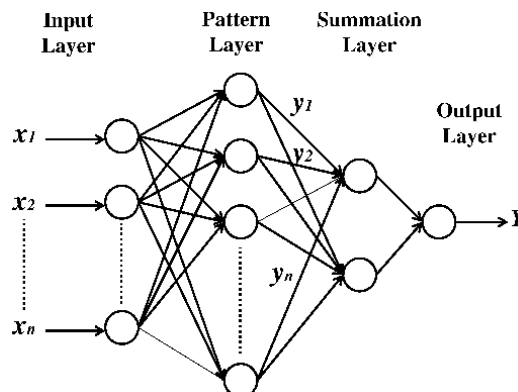
Figure 6. Schematic diagram of the structure of GRNN

Also, Specht clarified that the problem of the local minima is not encountered in the GRNN simulations. The input vector is contained in a specially created hidden neuron layer. The target value is assigned to the weight between the output neuron and the newly constructed hidden neuron. The main distinction between the two neural networks (GRNN and RBF) is how the values (w_{ij}) are calculated.

Extreme Learning Machines (ELM)

When training a single-layer feeder network (SLFN), algorithms such as back-propagation (BP) use specific rules to adjust the weights according to the particular batch in the training ensemble. The weights are randomly chosen in the ELM, the basic theory and algorithm of ELM are presented in [33]. Huang [34] concluded that SLFNs with random input weights could efficiently learn different training examples with minimal error. By choosing the input weights and the hidden layer biases, the SLFN can be treated as a linear system. The output weights are obtained analytically by a general inverse process for the hidden layer output matrices. This approach allows the ELM to run faster than the feed-forward algorithm [34].

Criteria for Measuring Performance

The performance efficiency evaluation criteria adopted in our study are respectively: coefficient of determination (R), Nash-Sutcliffe criteria (NSE), root mean square error (RMSE), mean absolute percentage error (MAPE). The governing Eqs. (5, 6, 7, and 8) of these criteria are stated as follows:

$$RMSE = \sqrt{\frac{\sum_{i=1}^{N}(\Delta T_{c_i}^{meas} - \Delta T_{c_i}^{pred})^2}{N-1}} \tag{5}$$

$$MAPE = \frac{1}{N}\sum_{i=1}^{N}\left|\frac{(\Delta T_{c_i}^{meas} - \Delta T_{c_i}^{pred})}{\Delta T_{c_i}^{meas}}\right| \times 100 \tag{6}$$

$$NSE = 1 - \frac{\sum_{i=1}^{N}(\Delta T_{c_i}^{meas} - \Delta T_{c_i}^{pred})^2}{\sum_{i=1}^{N}(\Delta T_{c_i}^{meas} - \overline{\Delta T_{c_i}^{meas}})^2} \tag{7}$$

$$R = \frac{\sum_{i=1}^{N}(\Delta T_{c_i}^{meas} - \overline{\Delta T_{c_i}^{meas}})(\Delta T_{c_i}^{pred} - \overline{\Delta T_{c_i}^{pred}})}{\sqrt{\sum_{i=1}^{N}(\Delta T_{c_i}^{meas} - \overline{\Delta T_{c_i}^{meas}})^2 \sum_{i=1}^{N}(\Delta T_{c_i}^{pred} - \overline{\Delta T_{c_i}^{pred}})^2}} \tag{8}$$

where meas and pred denote measured value and predicted value, respectively.

Two different models are created to predict ΔT_c, as revealed in Table 1.

Table 1. The two developed models inputs combination

Model Name	Models	Inputs	Output
RBFNN, GRNN, ELM	M1	Temperature, Time, Pressure, Grain size, Density and Young's modulus	Critical thermal shock temperature, ΔT_c
SE-RBFNN, SE-GRNN, SE-ELM	M2	Temperature, Grain size, Density and Young's modulus	

RESULTS AND DISCUSSION

The first model (M1) is developed using the six experimental inputs. For constructing the model (M2), the dimensions are reduced, and appropriate input variables are chosen using the Shannon entropy method. The considered model (M2) contains only four input variables with the highest entropy value using (M2-RBFNN, M2-GRNN, and M2-ELM).
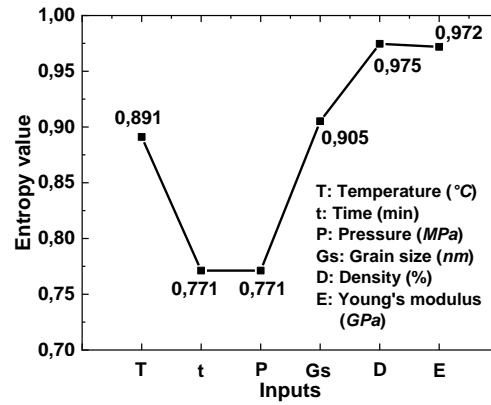
Figure 7. Inputs entropy values

The Shannon entropy of each input parameter is given in Figure 7. In the modeling, the inputs with higher entropy are more efficient compared to the other inputs. Therefore, the combinations of the selected four inputs (temperature, grain size, density, and Young's modulus) are chosen to build the ANN models (RBFNN, GRNN, and ELM). To develop the best model with the different types of ANNs, one must first determine the optimal number of hidden neurons, the appropriate transfer function, and the necessary iterations. These parameters are unavoidable for building and designing new models [35]. In this study, all models are built on the Matlab 2019b environment.

Based on the NSE values in the learning and testing phases, an overall comparison relates that all model sets obtained from (M1) and (M2) using RBFNN, ELM, and GRNN show acceptable performance for ΔT_c prediction. Except for the models obtained by ELM (R=0.0927 and R=0.5167), the NSE values are greater than 0.80. The overall performance results are shown in Table 2.

Table 2. Performance outcomes for M1 and M2 models

Model	Training				Testing			
	RMSE	MAPE	NSE	R	RMSE	MAPE	NSE	R
M1-BFNN	5.0791	0.3129	0.9878	0.9939	2.7209	0.2496	0.9979	0.9989
M1-GRNN	6.6238	0.6213	0.9793	0.9896	8.1436	1.0029	0.9810	0.9905
M1-ELM	30.8775	3.1904	0.5504	0.7419	73.7147	9.5556	-0.5569	0.0927
M2-BFNN	4.3751	0.3133	0.9910	0.9955	4.2613	0.4497	0.9948	0.9974
M2-GRNN	31.0358	2.9419	0.5458	0.7388	23.2261	2.5616	0.8454	0.9195
M2-ELM	36.8946	3.9150	0.3581	0.5984	50.5822	6.5242	0.2669	0.5167

M1 Model (6 inputs)

From Table 2, it is that M1 with six input variables generates high prediction accuracy of ΔT_c for the M1-RBFNN and M1-GRNN models in terms of RMSE, MAPE, NSE, and R. Looking at the values of RMSE (5.0791), MAPE (0.3129), NSE (0.9878), and R (0.9939) in the training phase, it can be seen that the M1-RBFNN model is very accurate compared to the M1-GRNN and M1-ELM models. Figure 8 shows the plots of the measured and predicted ΔT_c. Importantly, the overall performance of M1-RBFNN is high compared to the M1-GRNN and M1-ELM combinations.
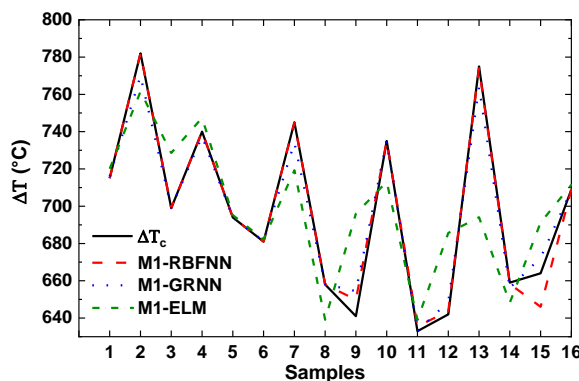
Figure 8. ΔT_c curves for the M2-RBFNN, M2-GRNN, and M2-ELM in the training phase
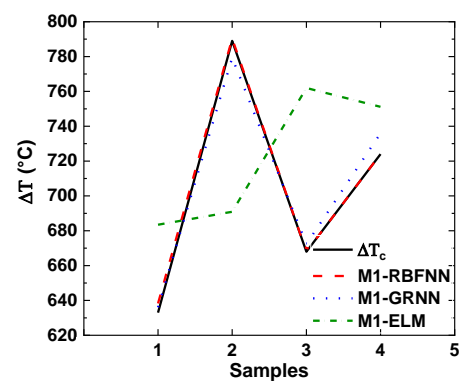
Figure 9. ΔT_c curves for the M1-RBFNN, M1-GRNN, and M1-ELM in the phase of testing

In addition, the trends of the predicted values show better agreement with the measured values than the other two models. In percentage of overall accuracy, M1-RBFNN outperforms the prediction performance at 0.86% and 79.47% for the M1-GRNN and M1-ELM models, respectively. In the test phase, the M1-RBFNN model outperforms M1-GRNN and M1-ELM by decreasing RMSE (2.7209), MAPE (0.2496) and increasing the performance criteria R (0.9989) and NSE (0.9979), respectively. Figure 9 represents the fit between the measured and predicted ΔT_c. The M1-RBFNN model combinations clearly outperform the M1-GRNN and M1-ELM model combinations in terms of generalization.
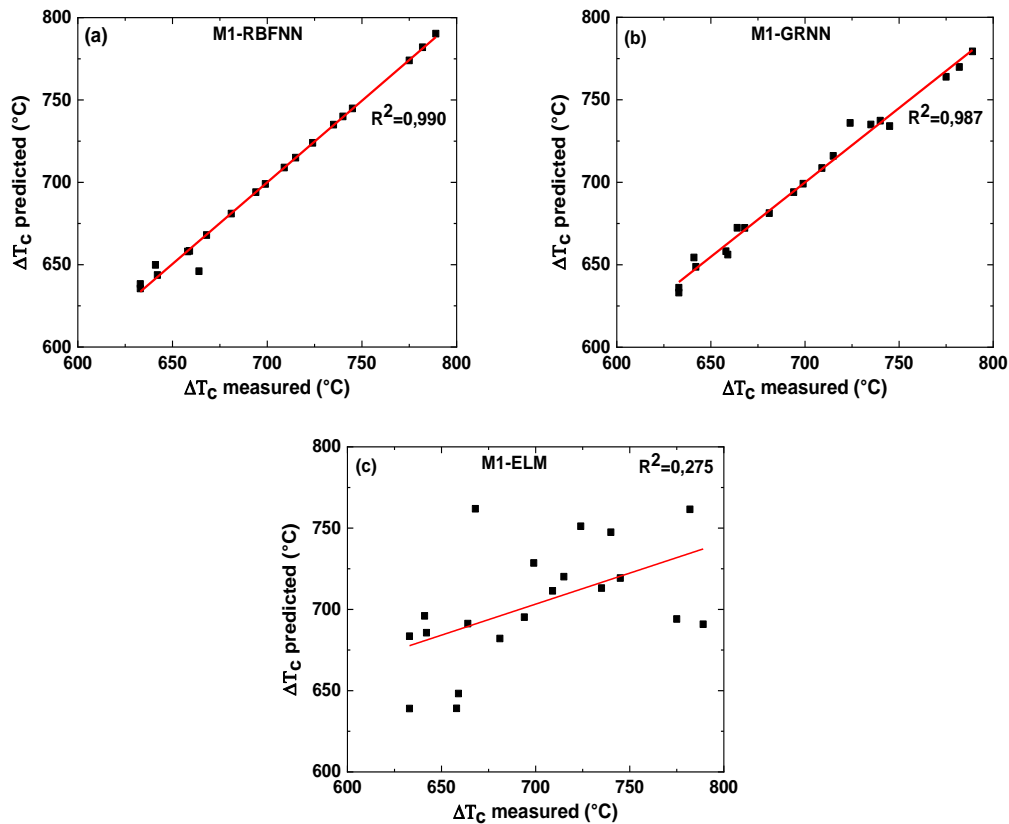
Figure 10. Measured and predicted ΔT_c with: (a) M1-RBFNN, (b) M1-GRNN, and (c) M1-ELM

The predicted values of ΔT_c using M1-RBFNN are neighboring the measured values, as shown in Figure 10(a) since their coefficient of determination (R^2) is very close to unity.

The poor predictive performance of M1-ELM can be attributed to the fact that the database used is concise, which limits the random identification of hidden biases and input weights. This can lead to an overfitting problem in the training phase. The ELM model requires an extensive database, and it is not available in our database, which led to insufficient performance factors in the testing phase.

M2 Model (4 inputs)

Using the Shannon entropy (SE) method for feature reduction with four combinations of inputs produces the greatest performance results in predicting ΔT_c. Furthermore, an explanation of the results reveals that for the predicted values of ΔT_c, M2-RBFNN in the learning phase, with RMSE (4.3751), MAPE (0.3133), NSE (0.9910), and R (0.9955), demonstrates merit over M2-GRNN and M2-ELM. Thus it appears as a reliable model.

The predicted values of the model that shows an excellent predictive advantage in the learning stage are presented in Figure 11 and Figure 13 (a). The global prediction results show that as the number of input variables decreases, the prediction of ΔT_c values is clearly improved.

Also, the predicted value models show greater agreement with the measured values than the two other models. In the percentage of overall precision, M2-RBFNN outperforms and gains predictive efficiency by up to 15.01% and 73.17% compared to the M2-GRNN and M2-ELM models, respectively. In the test phase, the M2-RBFNN model outperforms M2-GRNN and M2-ELM by decreasing the RMSE (2.7209), MAPE (0.2496) errors, and increasing the performance criteria NSE (0.9979) and R (0.9989), respectively.

The comparison between the measured and predicted ΔT_c is given in Figure 12. It is clearly visible that the M2-RBFNN combinations show superior generalization capabilities compared to the M2-GRNN and M2-ELM model combinations.
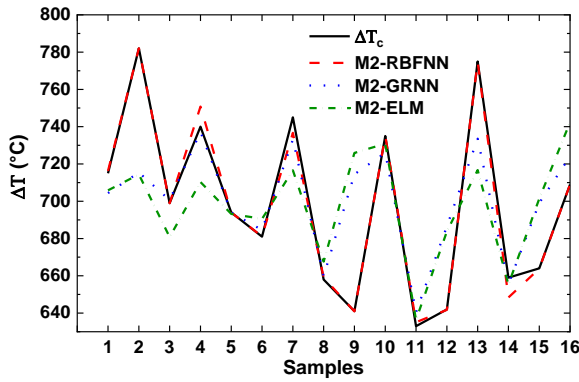
Figure 11. ΔT_c curves for the M2-RBFNN, M2-GRNN, and M2-ELM in the phase of training
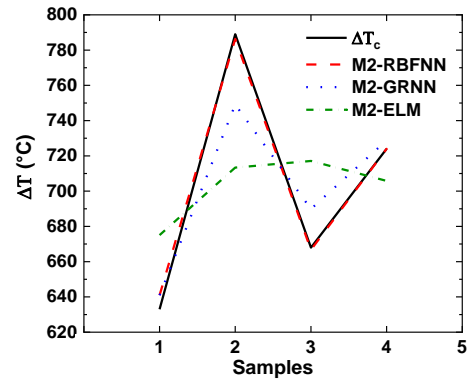
Figure 12. ΔT_c curves for the M2-RBFNN, M2-GRNN, and M2-ELM in the phase of testing

Figure 13(a) shows all predicted values of ΔT_c by using M2-RBFNN lie on the straight line since the coefficient of determination (R^2) is approximately equal to 1.
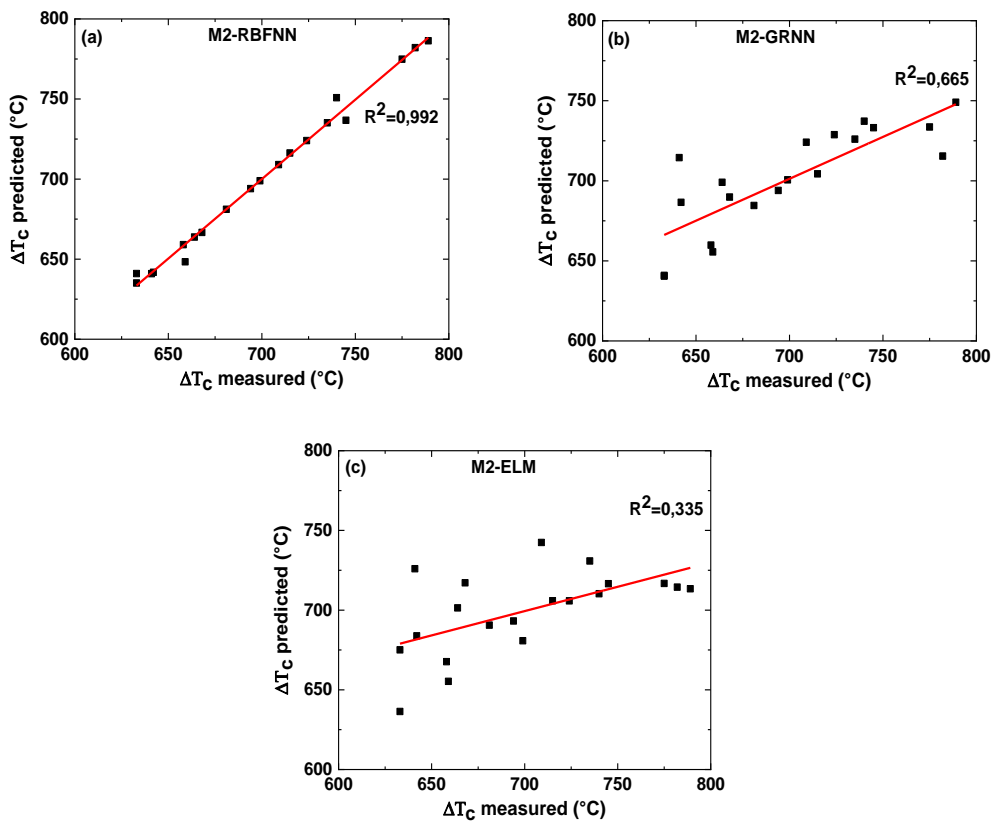
Figure 13. Measured and predicted ΔT_c with: (a) M2-RBFNN, (b) M2-GRNN, and (c) M2-ELM

According to reference [36], smaller values of MAPE prove that the model performance is high. Except for the ELM model, the obtained results show that all models are efficient according to this scale, see Table 2. Furthermore, the accuracy of performance in predicting ΔT_c increases as the number of input variables decreases. From Figure 14, the maximum predictive modeling errors of ΔT_c by using M2-RBFNN decrease by 39.48% compared to the M1-RBFNN model. All performance criteria prove that the M2-RBFNN model is superior to M1-RBFNN and M1-GRNN. Also, the outcomes reveal that the M2-RBFNN model with four combinations of inputs is the best model for predicting ΔT_c.
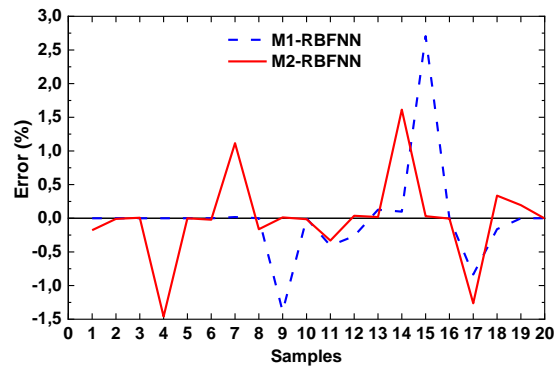
Figure 14. Difference in errors between the measured and predicted ΔT_c values based on M2-RBFNN and M1-RBFNN models

A two-dimensional approach, showing how the proposed models match the measured and predicted ΔT_c values, is employed to capture the performance details of the suggested predictive models (M1 and M2) employing different configurations of ANN (RBFNN, GRNN, and ELM). In Figure 15, the Taylor plot [37] is constructed to visualize the received information. The so-called Taylor plot is commonly used to compare accuracy various statistical measures in a single plot. The aim is to compare the similarity of the predicted and measured values by using a simple visual analysis process [34,38,39]. Looking at figure 15(a), it is apparent that the M1-RBFNN model (with six inputs) compared to the two other models (M1-GRNN and M1-ELM) is the closest to the measured values.
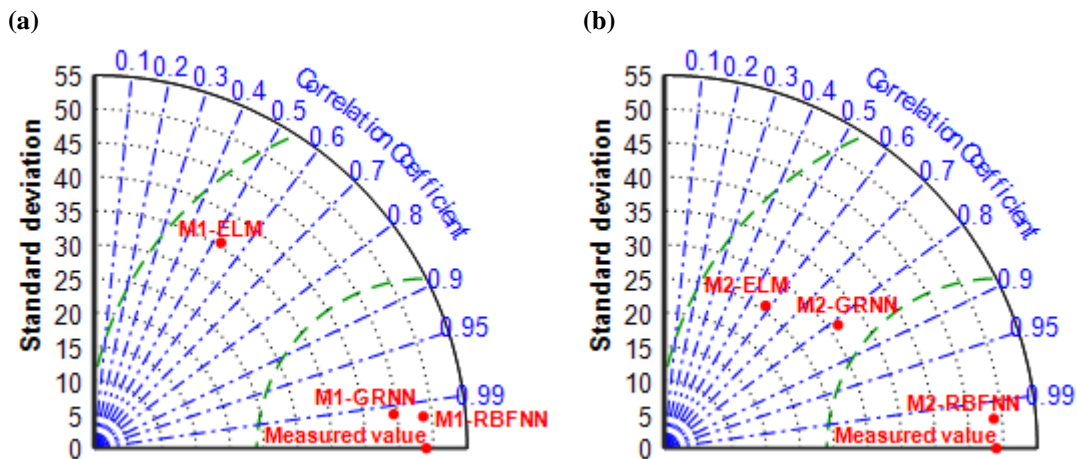
Figure 15. Taylor's diagram of ΔT_c predictive modeling using: (a) models M1 (6 inputs) and (b) models M2 (4 inputs)

The same observation is made for the proposed M2 models (M2-RBFNN, M2-GRNN, and M2-ELM) which are built with only four inputs, Figure 15(b). In general, the standard deviation (SD) analysis of the predicted values compared to the (SD) of the measured values allows us to evaluate the trend of the proposed model. If the (SD) of the predicted values exceeds the (SD) of the measured values, the model proposed tends to provide overestimated values and inversely. It is clear from Table 3 that the (SD) of the M2-RBFNN model is approximately equal to the SD of the measured values.

Table 3. The two developed models inputs combination

ΔT_c Measured values	M1 model			M2 model		
	M1-RBFNN	M1-GRNN	M1-ELM	M2-RBFNN	M2-GRNN	M2-ELM
Standard Deviation	48.979	48.752	44.445	35.601	48.785	31.411	25.785

RBFNNs demonstrated promise capabilities in nonlinear modeling, and this is not surprising as RBFNN has shown outstanding performance in engineering modeling. Table 4 shows the strong convergence between the predictive values based on the M2-RBFNN model and the experimental values. Also, it confirms the effectiveness of this model in predicting the critical temperature of the thermal shock of alumina.

Table 4. Experimental and predicted value of ΔTc

Experimental (ΔT_c)	M2-RBFNN (ΔT_c)
715	716.26
782	782.07
699	698.95
694	694.00
681	681.14
658	659.07
641	640.92
735	735.10
668	666.69
724	724.03
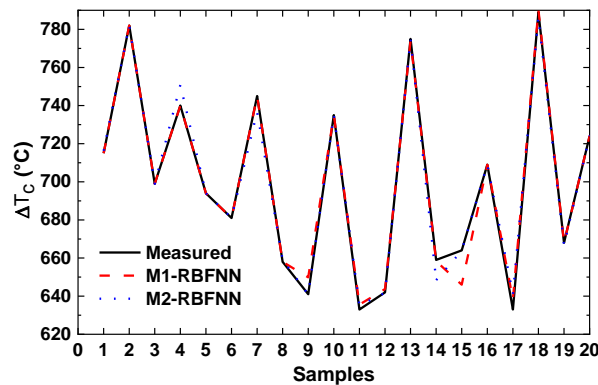
Figure 16. Comparison between the measured ΔT_c values with the M1-RBFNN and M2-RBFNN model values predicted

Finally, a comparative study is presented in Figure 16, in terms predicted values of ΔT_c utilizing M2-RBFNN and M1-RBFNN. Tthe proposed RBFNNs coupled with the Shannon entropy method as feature reduction technique (4 inputs) are found to have high predictive capabilities in predicting the critical thermal shock temperature (ΔT_c) compared to the single ANN model (6 inputs). The M2-RBFNN model is an excellent predictive model as it is built with reduced inputs, and its efficiency has been demonstrated in overcoming the smallness of the database.

CONCLUSION

In this paper, the combination of ANNs and the Shannon entropy method for predicting the critical thermal shock temperature (ΔT_c) are applied. The present research demonstrates the first use of SE-RBFNN models to predict ΔT_c.

The Shannon entropy method has been used in this study as feature reduction, and optimal inputs are used as inputs for different ANNs models (RBFNN, GRNN, and ELM). The main benefits of the Shannon entropy method are saving time and improving the accuracy of models in predictive modeling. For each of the proposed models (RBFNN, GRNN, and ELM), two different models are created, the first is a single model (M1-RBFNN, M1-GRNN, and M1-ELM), and the second is an hybrid model using the Shannon entropy method (M2-RBFNN, M2-GRNN, and M2-ELM). The predictive results show that the M2-RBFNN model has a high level of accuracy compared to single models for all the variables. The best accuracy of M2-RBFNN predictions is obtained when reducing the input from six to four input parameters of the artificial neural network using Shannon's entropy method. In contrast, low accuracy is observed for GRNN and ELM predictions using six input parameters.

ACKNOWLEDGMENT

REFERENCES

[1] G.Fantozzi, S. Gallet and J. Niepce, *Ceramic Science and Technology*, France: EDP Science, 2011.

[2] W. D. Kingery, "Factors affecting thermal stress resistance of ceramic materials," *Journal of the American Ceramic Society*, vol. 38, no. 1, pp. 3-15, 1955, doi: 10.1111/j.1151-2916.1955.tb14545.x.

[3]   D. P. H. Hasselman, "Unified theory of thermal shock fracture initiation and crack propagation in brittle ceramics," *Journal of the American Ceramic Society*, vol. 52, no. 11, pp. 600-604, 1969, doi: 10.1111/j.1151-2916.1969.tb15848.x.

[4]   F. Mignard, C. Olagnon, G. Fantozzi, P. Chantrenne and M. Raynauld, "Thermal shock behaviour of a coarse grain porous alumina," *Journal of Materials Science*, vol. 31, no. 8, pp. 2131-2138, 1996, doi: 10.1007/BF00356636.

[5]   F. Hugot and J. C. Glandus, "Thermal shock of alumina by compressed air cooling, " *Journal of the European Ceramic Society*, vol. 27, no. 4, pp. 1919-1925, 2007, doi: 10.1016/j.jeurceramsoc.2006.06.012.

[6]   X. Xu, S. Sheng, W. Yuan , and Z. Lin, "Effect of grain size on thermal shock property of alumina ceramic," *International Journal of Computational Materials Science and Engineering*, vol. 5, no. 1, p. 1650004, 2016, doi: 10.1142/S2047684116500044.

[7]   T. Bennouioua, Z. Malou, M. Hamidouche and G. Fantozzi, "Thermal shock behavior of a Soda Lime glass treated by Ion exchange," Glass Physics and Chemistry, vol. 46, no. 6, pp. 462-473, 2020, doi: 10.1134/S1087659620060048.

[8]   Z. Malou, M. Hamidouche, N. Bouaouadja, J. Chevalier and G. Fantozzi, "Thermal shock resistance of a soda lime glass," *Ceramics–Silikáty*, vol. 57, no. 01, pp. 39-44, 2013.

[9]   Z. Malou, M. Hamidouche, N. Bouaouadja and G. Fantozzi, "Analysis of a soda lime glass thermal shock resistance," *Ceramics-Silikáty*, vol. 55, no. 3, pp. 214-220, 2011.

[10]   M. Hamidouche, N. Bouaouadja, C. Olagnon and G. Fantozzi, "Thermal shock behaviour of mullite ceramic," *Ceramics International*, vol. 29, no. 6, pp. 599-609, 2003, doi: 10.1016/S0272-8842(02)00207-9.

[11]   R. Koker, N. Altinkok and A. Demir, "Neural network based prediction of mechanical properties of particulate reinforced metal matrix composites using various training algorithms," *Materials & Design*, vol. 28, no. 2, pp. 616-627, 2007, doi: 10.1016/j.matdes.2005.07.021.

[12]   H. S. Majdi, A. N. Saud and S. N. Saud, "Modeling the physical properties of gamma alumina catalyst carrier based on an artificial neural network," *Materials*, vol. 12, no. 11, p. 1752, 2019, doi: 10.3390/ma12111752.

[13]   A. Shokuhfar, M. N. Samani, N. Naserifar, P. Heidary and G. Naderi, "Prediction of physical properties of Al2TiO5-based ceramics containing micro and nano size oxide additives by using artificial neural network," *Mat.-wiss. u. Werkstofftech*, vol. 40, no. 3, pp. 169-177, 2009, doi: 10.1002/mawe.200900423.

[14]   C. Z. Huang, L. Zhang, L. He, J. Sun, B. Fang, B. Zou and X. Ai, "A study on the prediction of the mechanical properties of a ceramic tool based on an artificial neural network," *Journal of Materials Processing Technology*, vol. 129, no. 1-3, pp. 399-402, 2002, doi: 10.1016/S0924-0136(02)00701-X.

[15]   O. M. Elmabrouk and A. Kalkanli, "A neural network system for predicting the effect of Quartz and heat treatment on the corrosion properties of ceramic coating," *Journal of Multidisciplinary Engineering Science and Technology (JMEST)*, vol. 2, no. 1, pp. 1-5, 2015.

[16]   N. Altinkok, "Use of artificial neural network for prediction of mechanical properties of α-Al2O3 particulate-reinforced Al–Si10Mg alloy composites prepared by using stir casting process," *Journal of Composite Materials,* vol. 40, no. 9, pp. 779-796, 2006, doi: 10.1177%2F0021998305055547.

[17]   O. T. Adesina, T. Jamiru, I. A. Daniyan, E. R. Sadiku, O. F. Ogunbiyi, O. S. Adesina and L. W. Beneke, "Mechanical property prediction of SPS processed GNP/PLA polymer nanocomposite using artificial neural network," *Cogent Engineering*, vol. 7, no. 1, p. 1720894, 2020, doi: 10.1080/23311916.2020.1720894.

[18]   M. Çöl, H. M. Ertunç and M. Yılmaz, "An artificial neural network model for toughness properties in microalloyed steel in consideration of industrial production conditions," *Materials & Design*, vol. 28, no. 2, pp. 488-495, 2007, doi: 10.1016/j.matdes.2005.09.001.

[19]   J. Zhang, M. Yi, C. Xu and Z. Jiang, "Prediction of the mechanical properties of ceramic die material with artificial neural network," *IEEE International Conference on Intelligent Computing and Intelligent Systems*, Shanghai, 2009, doi: 10.1109/ICICISYS.2009.5357604.

[20]   H. Belghalem, M. Hamidouche, L. Gremillard, G. Bonnefont and G. Fantozzi, "Thermal shock resistance of two micro-structured alumina obtained by natural sintering and SPS," *Ceramics International*, vol. 40, no. 1, pp. 619-627, 2014, doi: 10.1016/j.ceram.int.2013.06.045.

[21]   H. Belghalem, M. Hamidouche, L. Gremillard, G. Bonnefond and G. Fantozzi, "Effect of spark plasma sintering of alumina nanopowder on the mechanical properties," *Journal of the Australian Ceramic Society*, vol. 53, no. 1, pp. 49-55, 2017, doi: 10.1007/s41779-016-0008-4.

[22]   M. Saadaoui, C. Olagnon and G. Fantozzi, "Evaluation of short crack R-curve behaviour of alumina under thermal shock loading," *Journal of Materials Science Letters*, vol. 15, no. 1, pp. 64-66, 1996, doi: 10.1007/BF01855615.

[23]   C. E. Shannon, "A mathematical theory of communication," *The Bell System Technical Journal*, vol. 27, no. 3, pp. 379-423, 1948, doi: 10.1002/j.1538-7305.1948.tb01338.x.

[24]   Y. Song and P. Wang, "A predictive model based on RBF neural network," *in Proc Sixth IASTED int Confon Intelligent Systems and Control*, pp. 380–383, 2004.

[25]   P. Chaber and M. Ławryńczuk, "RBF neural networks for modelling and predictive control: An application to a neutralisation process," *20th International Conference on Methods and Models in Automation and Robotics (MMAR)*, Miedzyzdroje, pp. 776-781, 2015, doi: 10.1109/MMAR.2015.7283974.

[26]   W. Kehe, Y. Yue, C. Bohao and W. Jinshui, "Research of wind power prediction model based on RBF neural network." *In 2013 International Conference on Computational and Information Sciences*, pp. 237-240, 2013, doi: 10.1109/ICCIS.2013.70.

[27] H. Haviluddin and I. Tahyudin, "Time series prediction using radial basis function neural network," *International Journal of Electrical and Computer Engineering (IJECE)*, vol. 5, no. 4, pp. 765-771, 2015, doi: 10.11591/ijece.v5i4.pp765-771.

[28] J. Moody and C. J. Darken, "Fast learning in networks of locally-tuned processing units," *Neural Computation*, vol. 1, no. 2, pp. 281-294, 1989, doi: 10.1162/neco.1989.1.2.281.

[29] S. Haykin, Neural networks and learning machines, 3rd ed. *Pearson Education India.*, 2009.

[30] D. F. Specht, "A general regression neural network," *IEEE Transactions on Neural Networks*, vol. 2, no. 6, pp. 568-576, 1991, doi:10.1109/72.97934.

[31] H. B. Celikoglu and H. K. Cigizoglu, "Public transportation trip flow modeling with generalized regression neural networks," *Advances in Engineering Software*, vol. 38, no. 2, pp. 71-79, 2007, doi: 10.1016/j.advengsoft.2006.08.003.

[32] B. Kim, D. W. Lee, K. Y. Park, S. R. Choi and S. Choi "Prediction of plasma etching using a randomized generalized regression neural network," *Vacuum*, vol. 76, no. 1, pp. 37-43, 2004, doi: 10.1016/j.vacuum.2004.05.018.

[33] G. B. Huang, Q. Y. Zhu and C. K. Siew, "Extreme learning machine: Theory and applications," *Neurocomputing*, vol. 70, no. 1-3, pp. 489-501, 2006, doi: 10.1016/j.neucom.2005.12.126.

[34] G. B. Huang, "Learning capability and storage capacity of two-hidden-layer feedforward networks," *IEEE Transactions on Neural Networks*, vol. 14, no. 2, pp. 274-281, 2003, doi: 10.1109/TNN.2003.809401.

[35] E. Olyaie, H. Z. Abyaneh and A. D. Mehr, "A comparative analysis among computational intelligence techniques for dissolved oxygen prediction in Delaware River," *Geoscience Frontiers*, vol. 8, no. 3, pp. 517-527, 2017, doi: 10.1016/j.gsf.2016.04.007.

[36] M. S. Gaya, M. U. Zango, L. A. Yusuf, M. Mustapha, B. Muhammad, A. Sani, A. Tijjani, N. Wahab and M. T. M. Khairi, "Estimation of turbidity in water treatment plant using Hammerstein-Wiener and neural network technique," *Indonesian Journal of Electrical Engineer*, vol. 5, no. 3, pp. 666-672, 2017, doi: 10.11591/ijeecs.v5.i3.pp666-672.

[37] Q. Wang, "Kernel principal component analysis and its applications in face recognition and active shape models," arXiv, 2012, doi: 10.48550/ARXIV.1207.3538.

[38] T. Zhou, F. Wang and Z. Yang, "Comparative analysis of ANN and SVM models combined with wavelet preprocess for groundwater depth prediction," *Water*, vol. 9, no. 10, p. 781, 2017, doi: 10.3390/w9100781.

[39] G. Elkiran, V. Nourani and S. I. Abba, "Multi-step ahead modelling of river water quality parameters using ensemble artificial intelligence-based approach," *Journal of Hydrology*, vol. 577, p. 123962, 2019, doi: 10.1016/j.jhydrol.2019.123962.